International Journal of Solids and Structures 338 (2026) 114096

Contents lists available at ScienceDirect

International Journal of Solids and Structures

journal homepage: www.elsevier.com/locate/ijsolstr

Achieving near yield isotropy with an offset-node hybrid lattice design

Xudong Huang [a], Penghui Yu [a], Peijie Zhang [a], Xueyan Chen [a,*], Huifeng Tan [a], Muamer Kadic [b]

[a] National Key Laboratory of Science and Technology on Advanced Composites in Special Environments, Harbin Institute of Technology, 92 Xidazhi Street, Harbin, 150001, PR China

[b] Université Marie et Louis Pasteur, SUPMICROTECH, Institut FEMTO-ST, 25000 Besançon, France

ARTICLE INFO

Keywords:
Elastic isotropy
Yield anisotropy control
Mechanical metamaterial
Stretching-dominated

ABSTRACT

Lattice materials offer highly customizable mechanical properties, but their practical application is often limited by pronounced anisotropy, which makes them unsuitable for non-deterministic, multi-axial loading environments. While significant progress has been made in achieving elastic isotropy, controlling yield anisotropy, critical for nonlinear large deformations, remains a challenge. To address this, we introduce a novel design strategy that offsets the central node of a cubic unit cell along its spatial diagonal, creating a tunable hybrid architecture that interpolates between Simple Cubic and Body-Centered Cubic configurations. We systematically map the design space defined by this offset ratio and relative density to tailor elastic isotropic properties. Crucially, numerical and experimental results reveal that this ratio also provides precise control over yield anisotropy. We demonstrate a high degree of yield isotropy, achieving a near-ideal anisotropy ratio of 1.05 at a relative density of 0.25. This performance represents a notable advancement in the development of isotropic lattice architectures within the nonlinear regime. This exceptional isotropy remains stable across increasing densities, confirming the design's robustness. Combined with high inherent stiffness and strength, these near-isotropic lattices are prime candidates for advanced load-bearing applications under uncertain loading conditions. Our strategy provides a powerful method for controlling anisotropy across linear and nonlinear regimes, with promising applications in aerospace, biomedical engineering, and beyond.

1. Introduction

Over the past decades, lattice materials, which are defined by the periodic repetition of fundamental unit cells, have garnered widespread interest for their remarkable, tunable mechanical properties (Liu et al., 2025b, 2024a; Wang et al., 2024; Liu et al., 2025a), such as low density (Wei et al., 2024b; Schaedler et al., 2011; Mizzi et al., 2025), high specific stiffness and strength (Zheng et al., 2014; Chen et al., 2020a; Yan et al., 2024), superior energy absorption (Yu et al., 2025; Zhang et al., 2025a, 2023; Tan et al., 2026; Zhang et al., 2025b),programmable deformation behavior (Wei et al., 2024a; Yu et al., 2024; Dudek et al., 2025; Tan et al., 2024b,a), and adjustable Poisson's ratios (Chen et al., 2020b). Crucially, these attributes stem from the geometry of the unit cell rather than the properties of the base material (Chen and Tan, 2018; Jiao et al., 2023). Based on their geometrical profile, lattice materials can be classified as bending-dominated or stretching-dominated types (Deshpande et al., 2001a,b). Bending-dominated lattices typically exhibit superior nonlinear-stage stability, whereas stretching-dominated lattices deliver higher specific stiffness and strength, both scaling linearly with relative density. However, the unhomogenised porous architecture of both configurations often induces pronounced anisotropy, preventing consistent performance under variable loading directions and thus limiting their use in non-deterministic service conditions (Chen et al., 2024).

Tailoring strut cross-sections to adjust the bending-to-axial stiffness ratio is a common method for regulating elastic anisotropy, particularly in hollow truss and shell lattice materials. Tancogne et al. demonstrated that by adjusting the inner-to-outer diameter ratio of hollow tubes, three fundamental cubic truss lattices achieve elastic isotropy across the entire relative density range of 0.01 to 0.5 (Tancogne-Dejean and Mohr, 2018a). Bonatti et al. further demonstrated that tuning the parameters of surface-definition functions within anisotropic structure families yields elastically isotropic shells (Bonatti and Mohr, 2019). Chen et al. devised a novel class of simple cubic (SC) tubular lattices that combine high mechanical performance with reduced loading-direction sensitivity and an irregular yet stable post-yield response (Chen et al., 2022a). Ma et al. introduced a family of variable-thickness triply periodic minimal surface (TPMS) shell lattices with isotropic stiffness, designed via a strain–energy-based optimization algorithm (Ma et al., 2021). Zhao et al. employed artificial neural network optimization to regulate elastic isotropy, designing a bamboo-inspired body-centered

* Corresponding author.
E-mail address: chenxueyan@hit.edu.cn (X. Chen).

https://doi.org/10.1016/j.ijsolstr.2026.114096
Received 25 December 2025; Received in revised form 12 May 2026; Accepted 18 May 2026
Available online 1 June 2026

cubic (BCC) lattice composed of tapered and hollow struts (Zhao et al., 2023).

Alternatively, elastic isotropy can be achieved by combining multiple anisotropic configurations in carefully chosen proportions. Gurtner et al. theoretically proposed a novel optimal isotropic 3D truss lattice by combining simple cubic and BCC truss architectures (Gurtner and Durand, 2014). Similarly, Xu et al. achieved elastic isotropy by either assembling two basic units with complementary stiffness along different spatial directions or applying symmetric operations to a single unit with partial symmetry to construct a new representative unit (Xu et al., 2016). Tancogne et al. identified specific elastically isotropic truss structures by combining elementary cubic lattices, achieving reduced initial yield anisotropy compared to octet trusses (Tancogne-Dejean and Mohr, 2018b). Berger et al. were the first to pinpoint mechanical metamaterials that reach the theoretical limit of isotropic elastic stiffness by combining SC and octet plate lattices (Berger et al., 2017). Laterly, Tancogne et al. experimentally validated this concept and developed a theoretical design map for cubic-symmetric elastically isotropic plate lattices (Tancogne-Dejean et al., 2018). Chen et al. proposed a BCC–SC truss lattice that balances the complementary properties of BCC and SC geometries to achieve near-perfect elastic and yield isotropy (Chen et al., 2022b). However, as a bending-dominated structure, it exhibits slightly lower specific strength and stiffness than its stretching-dominated counterparts. Wang et al. introduced a bioinspired bilayer hybrid truss–plate hierarchy that achieves both elastic isotropy and enhanced modulus by integrating truss and plate motifs to balance mechanical responses along orthogonal directions, demonstrating the effectiveness of multiscale structural hybridization (Wang et al., 2023). Liu et al. propose a novel approach to achieving isotropic elasticity by combining different TPMS shell lattices with complementary anisotropic behaviors into a hierarchical structure (Liu et al., 2024b). Jing Zhang et al. achieved isotropy by combining different TPMS lattices, with varying axial and diagonal stiffness, via Boolean fusion, enabling mutual property compensation (Zhang et al., 2024). However, most research to date addresses only elastic isotropy, regulating anisotropy during the nonlinear stage typically necessitates complex, hard-to-fabricate configurations or incurs trade-offs in strength and stiffness, falling short of stringent nonlinear-performance requirements.

To address this challenge, we propose a novel design strategy that, unlike conventional lattices with uniform symmetrical geometries, introduces deliberate offset asymmetry to achieve elastic isotropy and regulate nonlinear-stage anisotropy, while preserving both stiffness and strength. Specifically, we demonstrate the regulatory capability of non-uniform distributions by embedding BCC truss lattices into eight unequally divided cuboids, framed by SC truss lattices. The resulting non-uniform structure exhibits significantly enhanced near-isotropic behavior in the nonlinear stage compared to traditional uniform elastic-isotropic lattices. The effects of relative density and offset ratio on mechanical properties, particularly the loading-direction dependence in both linear and nonlinear stages, are investigated through numerical simulations. These findings are further validated by uniaxial compression tests on 3D-printed samples with a relative density of 0.25, fabricated along the [100] and [110] crystallographic directions, offering a new paradigm for regulating anisotropy in the nonlinear regime of lattice materials.

2. Metamaterial design

2.1. Structural design concept

Conventional lattice designs enforce symmetry at both the unit-cell and sub-unit-cell levels,for instance, through a symmetric 2 × 2 arrangement with mirror symmetry (Fig. 1a). While this guarantees perfect structural uniformity, it significantly restricts the geometric design space, making it challenging to simultaneously tailor multiple mechanical properties, such as achieving both elastic and yield isotropy. To introduce additional design flexibility, the conventional uniform splitting approach is modified to a non-uniform mode by introducing an offset factor, $\alpha = \frac{L_1}{L}$, which allows precise control over the position of the coincident point along the diagonal within the sub-unit-cell. Here, L_1 is the distance from the coincident point to the nearest symmetric line, and L is the overall length of the sub-unit-cell. Consequently, the square regions below and above the diagonal scale inversely, one shrinking as the other grows, while the adjoining rectangles acquire new aspect ratios. Structural unit cells are then generated by populating these rectangles according to their adjusted aspect ratios.

To evaluate the effectiveness of the proposed strategy in controlling anisotropy during the non-linear response of 3D lattice structures, we generalize the 2D plane division method to three-dimensional space. Conventionally, a uniformly distributed lattice can be represented as a cube partitioned into eight identical sub-cubes, forming the structural framework into which the lattice profile is embedded. In contrast, our approach offsets the cutting planes along the three principal axes, producing eight cuboids of varying dimensions. Each cuboid is then filled with a lattice whose length-width-height ratios match its geometry, resulting in a non-uniform, variable-distribution structure.

As an illustrative example, we combine BCC and SC truss lattices: BCC lattices fill the original frame regions, while SC lattices replace the frame elements. Owing to the overall symmetry, the dashed box in Fig. 1b represents one-eighth of the unit cell. Let the side length of this octant be L, and the distance from the central node to the lower-left-front plane be $L/2$. Denote the BCC strut diameter by D_1 and the SC strut diameter by D_2. By fixing the ratio D_1/D_2 at an optimal value, the well-known elastic-isotropic BCC-SC truss lattice is attained (see Fig. 1b). Under our offset strategy, that same nodal-to-face distance becomes L_1. The full unit cell is then assembled by mirroring this octant across the three principal planes, yielding a cube of side length $2L$ in which the spacing between the two horizontal struts is $2L_1$ (Fig. 1b). By varying the offset factor α, we achieve different spatial distributions, and by adjusting D_1/D_2, we combine anisotropic substructures in controlled volume ratios to realize overall elastic isotropy in the offset configuration. For example, elastic isotropy is realized for α values ranging from 0.1 to 0.5, with $\alpha = 0.5$ reverting to the conventional BCC–SC truss lattice. Fig. 1d further illustrates the capability of our offset strategy to control yield isotropy through variations in α. Whereas the original lattice exhibits a yield-strength anisotropy ratio of approximately 1.3, the optimal offset configuration reduces this ratio to about 1.05. Here, the yield strength anisotropy ratio is defined as the ratio of the maximum to the minimum yield strength ($\sigma_y^{\max}/\sigma_y^{min}$) calculated across all possible loading orientations in three-dimensional space. This significant improvement validates our design concept; further details are presented in the following section.

2.2. Relative density

This section examines the crucial relationship between relative density ρ^* and two key dimensional ratios in lattice materials: the offset distribution factor α and the aspect ratio D_1/L and D_2/L. For the non-uniform BCC-SC truss lattice (NBCC-SC), the relative density is defined as the volume V of solid material divided by the total unit cell volume.

$$\rho^* = \frac{V_{\mathrm{NBCC-SC}}}{L^3}. \tag{1}$$

First, the relative density of the SC truss structure is defined, where V_{SC} is calculated as the total volume of three orthogonal cylindrical struts (diameter D_2, aligned with the unit cell axes) minus the volume of overlapping regions at nodes.

$$\rho^*_{SC} = \frac{3}{4}\pi\left(\frac{D_2}{L}\right)^2 - C_1\left(\frac{D_2}{L}\right)^3 \tag{2}$$

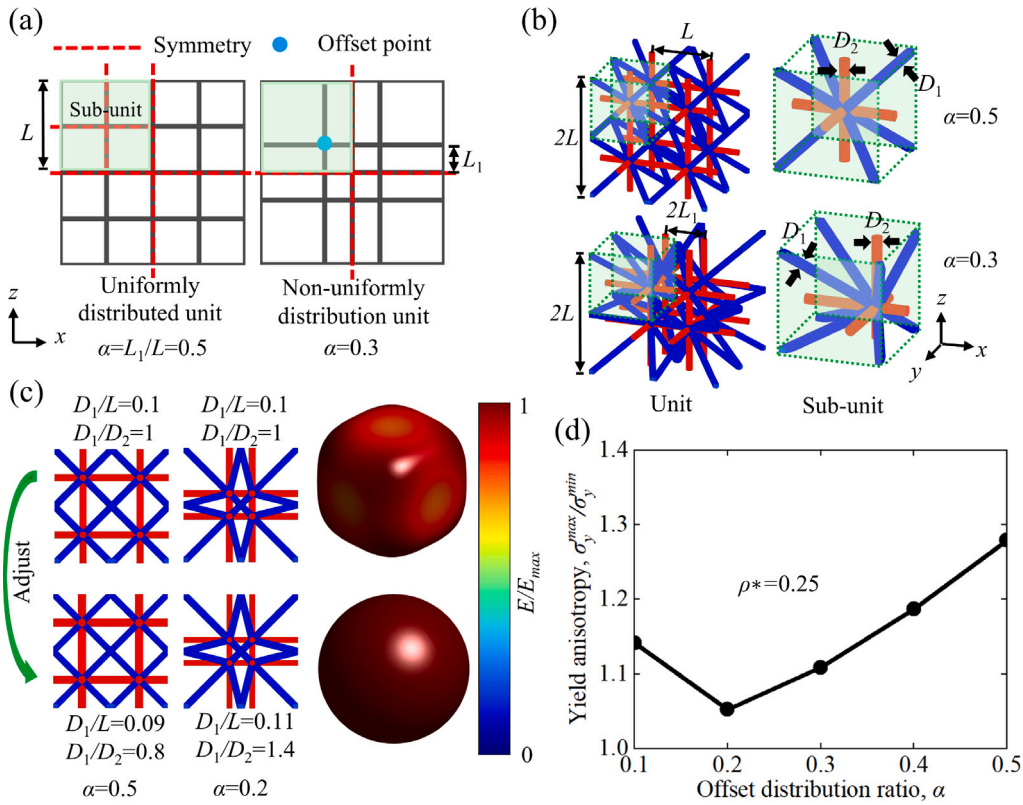

Fig. 1. A general non-uniform distribution strategy for tailoring mechanical properties: (a) schematic comparison of 2D planar non-uniform splitting versus conventional uniform splitting. (b) Geometric depiction of the standard BCC–SC truss lattice alongside the newly generated, offset parameter-dependent hybrid truss lattice. (c) Example demonstrating that the generated structure can achieve elastic isotropy by varying the diameter ratio.(d) Evolution of yield-strength anisotropy for the proposed truss lattice at a relative density of 0.25 as a function of the offset coefficient.

The constant $C_1 = 1.414$ compensates for overlapping volumes at SC nodal intersections. This value was numerically determined through 3D CAD modeling. The volume of the offset BCC structure, denoted as V_{NBCC}, is calculated as the sum of the volume of a central cylindrical strut aligned along the [111] direction with diameter D_1, and six oblique cylindrical rods also of diameter D_1, minus the overlapping volumes at their intersections.

$$\rho^*_{NBCC} = \frac{\sqrt{3}}{4}\pi\left(\frac{D_1}{L}\right)^2\left[1+\sqrt{2\alpha^2+(1-\alpha)^2}+\sqrt{\alpha^2+2(1-\alpha)^2}\right] - C_2\left(\frac{D_1}{L}\right)^3 \tag{3}$$

The calculated constant C_2 for the offset BCC structure varies with the parameter α, and the corresponding values are plotted in Fig. 2a.

The volume of the proposed structure is given by the sum of the offset BCC lattice volume and the SC lattice volume, minus their overlapping volume. Accordingly, its relative density is calculated as follows:

$$\rho^*_{NBCC-SC} = \rho^*_{SC} + \rho^*_{NBCC} - C_3\left(\frac{D_2}{L}\right)^3 \tag{4}$$

$$C_3 = Ae^{-\left(\frac{D_2}{L}\right)/B} + E \tag{5}$$

The constant C_3 exhibits variation with geometrical ratios α and D_2/L in the proposed structures, as illustrated in Fig. 2b. It clearly decreases with increasing values of either α or D_2/L.

3. Numerical simulation

3.1. Evaluation of elastic isotropy

The constitutive relation for the lattice structure is given by $\sigma = C:\varepsilon$, where σ is the stress tensor, ε is the strain tensor, and C is the effective elasticity tensor. Under simple cubic symmetry, the fourth-order elasticity tensor C exhibits three independent components: C_{11}($C_{1111} = C_{2222} = C_{3333}$), C_{12} ($C_{1122} = C_{1133} = C_{2233}$, and symmetry-equivalent permutations), C_{44} ($C_{2323} = C_{1313} = C_{1212}$, and symmetry-equivalent permutations). These components adopt the compact Voigt notation (Voigt, 1910), simplifying the constitutive relation to

$$\boldsymbol{C} = \begin{bmatrix} C_{11} & C_{12} & C_{12} & 0 & 0 & 0 \\ C_{12} & C_{11} & C_{12} & 0 & 0 & 0 \\ C_{12} & C_{12} & C_{11} & 0 & 0 & 0 \\ 0 & 0 & 0 & C_{44} & 0 & 0 \\ 0 & 0 & 0 & 0 & C_{44} & 0 \\ 0 & 0 & 0 & 0 & 0 & C_{44} \end{bmatrix} \tag{6}$$

Young's modulus E, shear modulus G, and the Zener's ratio Z can be expressed as functions of the stiffness tensor (Bückmann et al., 2014):

$$E = \frac{C_{11}^2 + C_{11}C_{12} - 2C_{12}^2}{C_{11}+C_{12}} \tag{7}$$

$$G = C_{44} \tag{8}$$

$$Z = \frac{2C_{44}}{C_{11}-C_{12}} \tag{9}$$

Z quantifies elastic anisotropy in cubic crystals, where $Z = 1$ indicates perfect elastic isotropy.

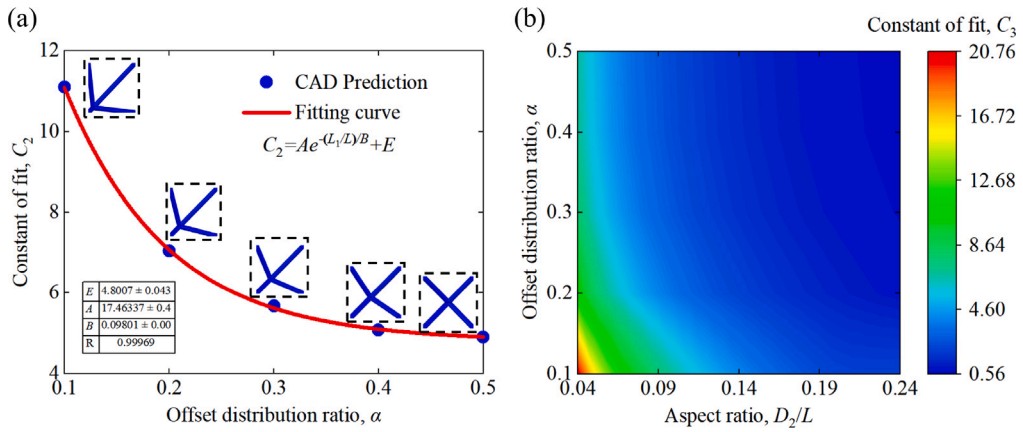

Fig. 2. The fitting plots of constants C_2 and C_3, (a) Compensation constant C_2 for calculating relative density after non-uniform distribution of BCC structure; (b) Compensation constant C_3 for the combination of BCC and SC structures in variable-distribution BCC-SC structure.

The propagation of fluctuations in complex periodic systems is usually addressed using Bloch's theorem, which involves applying periodic boundary conditions to the discretized unit cells (Maurin et al., 2017). Based on the Christoffel equation for elastic waves, the independent stiffness constants can be derived from the equivalent mass density and the phase velocities in a chosen propagation direction. Specifically, all stiffness constants are determined by three phase velocities,v. For propagation along the [110] direction, consider: a pure shear wave S_1 polarized along [001], and two waves with mixed polarization in the xy-plane—the quasi-longitudinal (L) wave and the quasi-shear (S_2) wave. In this case, the Christoffel equation yields (Tsang and Park, 1983):

$$C_{44} = \rho \cdot v_{s1}^2 \tag{10}$$

$$C_{12} = \rho \cdot v_L^2 - v_{s1}^2 - v_{s2}^2 \tag{11}$$

$$C_{11} = \rho \cdot v_L^2 - v_{s1}^2 + v_{s2}^2 \tag{12}$$

Substituting Eqs. (10), (11) and (12) into Eq. (9), a new expression for evaluating elastic isotropy is obtained:

$$Z = \frac{v_{s1}^2}{v_{s2}^2} \tag{13}$$

3.2. Numerical modeling

To obtain the key velocities, eigenfrequency analyses were carried out in the commercial finite element package COMSOL Multiphysics. Each truss lattice unit cell was discretized with at least 80,000 linear tetrahedral elements (type C3D10M) to ensure sufficient accuracy (see Fig.S1). Bloch periodic boundary conditions were then imposed on the representative unit cell model (Maurin et al., 2017). These specialized boundary conditions are used to simulate periodic structures by enforcing that the displacement fields at opposite boundaries remain identical, subject to a phase shift defined by the wave vector k. The base material PA12 was treated as isotropic, with a Young's modulus of 0.95 GPa, Poisson's ratio of 0.4, and a density of 1000 kg/m^3. These properties were derived from tensile experiments (see Fig.S2). The materials used in both the simulation and experimental printing in this paper are PA12. The plasticity constitutive model is the exponential hardening model, which is used to describe the mathematical law that the yield stress of the material increases with the increase of plastic deformation after it enters the plastic state. Because this growth curve is in an exponential form, it first increases rapidly and then tends to stabilize. Finally, eigenfrequencies were computed for a small wavenumber long the [110] direction.

To compare the wave numbers along all directions of the 3D crystal, and given that determining whether the elastic stage is isotropic only requires comparing f_1 and f_2, the 3D directional dependence of the characteristic frequencies f_1 and f_2 was visualized. The first and second-order frequencies under the same relative density but different distribution coefficients a were plotted, as shown in Fig. 3. Based on the formula derivation, we achieved isotropic behavior in the elastic stage for BCC-SC structures with different distributions by adjusting D_1/D_2. Specifically, the first and second characteristic frequencies were nearly identical, and a value of $Z = 1$ could be obtained according to the formula. Meanwhile, the characteristic frequencies obtained with wave numbers along different directions of the 3D crystal were also almost consistent, which manifested as nearly isochromatic spheres in the figure.

After determining the geometric parameters that yield elastic isotropy, unit cell models of the proposed non-uniform BCC–SC lattices were built in ABAQUS for relative densities from 0.05 to 0.25 to extract their mechanical properties. The base material PA12 was modeled as isotropic elasto-plastic, with the same elastic properties used in the eigenfrequency analyses and an isotropic strain-hardening behavior. The plasticity parameters, including a 0.2% offset yield strength of 16.6 MPa and the subsequent hardening behavior, were extracted directly from experimental tensile tests (see Fig.S2). To account for material failure, a ductile damage initiation criterion was integrated with a fracture strain of 0.35 and a stress triaxiality of −1/3 (Daynes and Feih, 2025). The damage evolution followed a linear softening law, with element removal occurring at a maximum degradation of 95%, corresponding to a failure displacement of 0.75 mm. According to Abaqus analysis user's guide (2020), the failure displacement is regularized by the product of the fracture strain and a characteristic length L_C. The characteristic length is prescribed based on the minimum element volume$V_{\min}$ through the relation $L_C = \frac{1}{2}\sqrt[3]{V_{\min}}$. To address the nodal complexity, the non-uniform BCC–SC structures were discretized with at least 188,328 second-order tetrahedral solid elements (C3D10) to ensure computational accuracy. For comparison, conventional homogeneously distributed BCC–SC and BCC lattices were also modeled; owing to its higher symmetry the BCC lattice was meshed with at least 50,000 first-order hexahedral solid elements (C3D8R). All unit cells maintained 200 mm side length, with geometric parameters adjusted per target density and isotropy-optimized ratios. Periodic boundary conditions were implemented via linear constraint equations pairing nodes on opposing faces to reduce computational cost (Li and Wongsto, 2004). Elastic moduli and Poisson's ratio were extracted from small-strain simulations, uniaxial compression along a principal direction, pure shear, and hydrostatic loading. To assess the influence of loading direction on yield strength and large-deformation behavior, additional compression simulations were performed along 31 orientations up to a

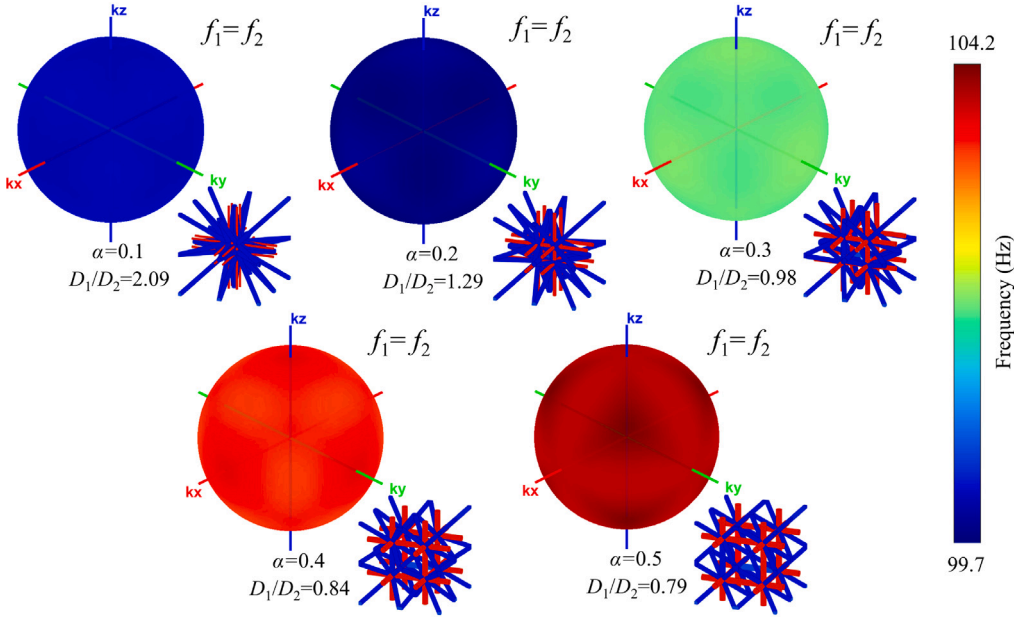

Fig. 3. Contour plots of the first and second characteristic frequencies of the variable-distribution BCC-SC structure along different directions. The plots correspond to a fixed Bloch wave vector magnitude $|K| = 0.1\pi/L$ (with varying directions), a relative density of 0.1, different distribution coefficients, and the geometric dimension ratio D_1/D_2 that satisfies elastic isotropy.

nominal strain of 0.3. The initial yield strength was defined as the axial stress at which the permanent strain reaches 0.2%.

To further reveal the large deformation response of the lattice structures, 3 × 3 × 3 multi-cell models were developed. The [100] configuration consisted of approximately 5 million solid elements, whereas the [110] model was discretized with about 10 million elements to ensure numerical accuracy. The same element type used in the unit-cell simulations was retained. The lattice assembly was placed between two rigid platens, and an explicit dynamic integration scheme was employed to capture the complex fracturing and contact behavior. General self-contact was implemented with a friction coefficient of 0.2. During the simulation, the bottom platen was fully constrained, while the top platen applied a displacement-controlled loading up to 20% densification. To maintain a quasi-static response, the ratio of kinetic energy to internal energy was kept strictly below 1% throughout the loading process.

3.3. Elastic mechanical properties

Fig. 4 and Fig.S3 presents a contour map of the Zener's ratio versus the geometric ratios D_1/D_2 and α for relative densities between 0.05 and 0.25, computed from the eigenfrequency results using the preceding equation. Generally, the Zener's ratio generally increases with both geometric parameters. Elastic isotropy is attainable across this range by matching D_1/D_2 and α. When relative density ranges from 0.05 to 0.15, the relationship between α and its isotropy-achieving D_1/D_2 counterpart remains nearly constant. As α increases from 0.1 to 0.5, the required D_1/D_2 ratio decreases nonlinearly: from approximately 2.0 at α = 0.1, to 1.3 at α = 0.2, to about 1 at α = 0.3, and 0.85 at α = 0.4. For the classical BCC-SC structure (α = 0.5), the isotropy ratio D_1/D_2 ≈ 0.8 closely matches findings of the exist Tancogne-Dejean and Mohr (2018b), validating accuracy of the method.

At a relative density of 0.2, geometric parameters achieving elastic isotropy follow similar trends to lower densities except at α = 0.1, where D_1/D_2 decreases significantly to about 1.6 due to volume overlap at nodes between offset BCC and SC truss lattices. For α = 0.2–0.5, isotropy-achieving D_1/D_2 ratios exhibit minimal variation. At a relative density of 0.25 and α = 0.1, the structure becomes highly compact and the geometric-regulation strategy used here is no longer applicable (See Fig.S3). Consequently, structures at a relative density of 0.25 were analyzed only for α between 0.2 and 0.5, which provides well-defined geometries for investigating elastic isotropy in the inhomogeneously distributed BCC–SC designs.

Having established that perfect elastic isotropy can be achieved by tuning geometric parameters across a range of relative densities, it remains essential to investigate how these parameters affect other elastic mechanical properties. Fig. 5 presents a contour plot of the effect of the inhomogeneous distribution strategy on normalized Young's modulus, specific shear modulus, specific bulk modulus, and Poisson's ratio for the elastic isotropic BCC–SC family. In the plot, each horizontal row displays the variation of these normalized properties at a fixed relative density across different offset distribution factor α, while each vertical column shows their variation with relative density at a fixed α. Overall, the normalized moduli increase with relative density. For relative densities between 0.05 and 0.25, inhomogeneous distribution of BCC–SC variants reduces specific mechanical properties versus a uniform lattice: Young's and shear moduli by 1%–12%, the bulk modulus by 1%–23%, and Poisson's ratio by 0%–7%. Significant reductions occur in variants NBCC-SC (α = 0.1) and NBCC-SC (α = 0.2), while NBCC-SC (α = 0.3) and NBCC-SC (α = 0.4) are less affected, changing by less than 5%.

Specifically, Fig. 6 compares the elastic moduli of the elastically isotropic NBCC–SC truss lattices (optimized for isotropic yield strength; see next section) and BCC-SC truss lattices with those of a conventional BCC lattice at each relative density. For enhanced readability, the corresponding normalized elastic properties are provided in Fig.S4. The BCC lattice displays pronounced anisotropy: the relative elastic modulus is lowest along the [100] direction and highest along [111], The relative shear modulus is the highest on the [100] plane and the lowest in the [110] direction. These directional disparities hinder the BCC lattice from realizing its optimal mechanical performance under uncertain loading. By contrast, the geometrically tuned NBCC–SC lattice behaves isotropically and is therefore better suited to such working conditions. As relative density increases, the relative Young's, shear, and bulk moduli of the NBCC–SC lattices and the upper-bound BCC lattices rise nearly linearly, indicating stretching-dominated behavior, whereas the lower-bound BCC lattices scale nonlinearly with relative density, reflecting bending-dominated behavior. At a relative density of

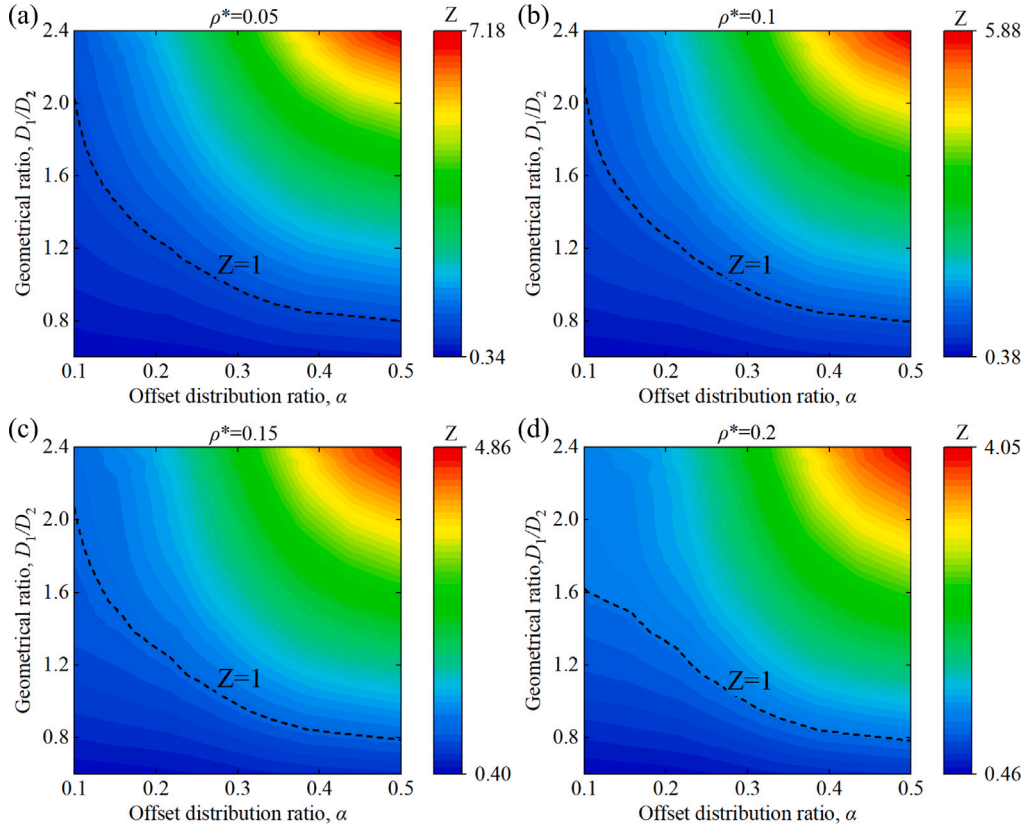

Fig. 4. Contour plots of elastic anisotropy for NBCC–SC lattices at different "α " and D_1/D_2 values, for relative densities ranging from (a-d) 0.05 to 0.20.

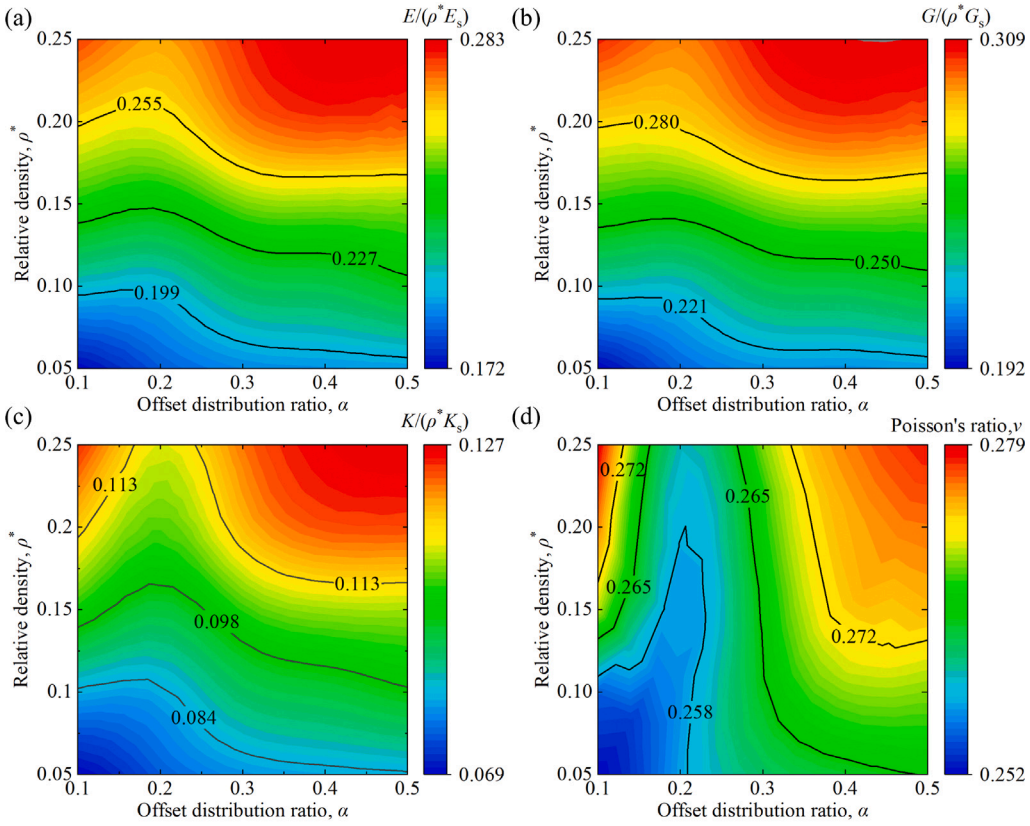

Fig. 5. The influence of the offset distribution ratio α on the mechanical properties of elastic isotropic lattices for a given range of relative densities: (a) relative elastic modulus, (b) relative shear modulus, (c) relative bulk modulus, and (d) Poisson's ratio.

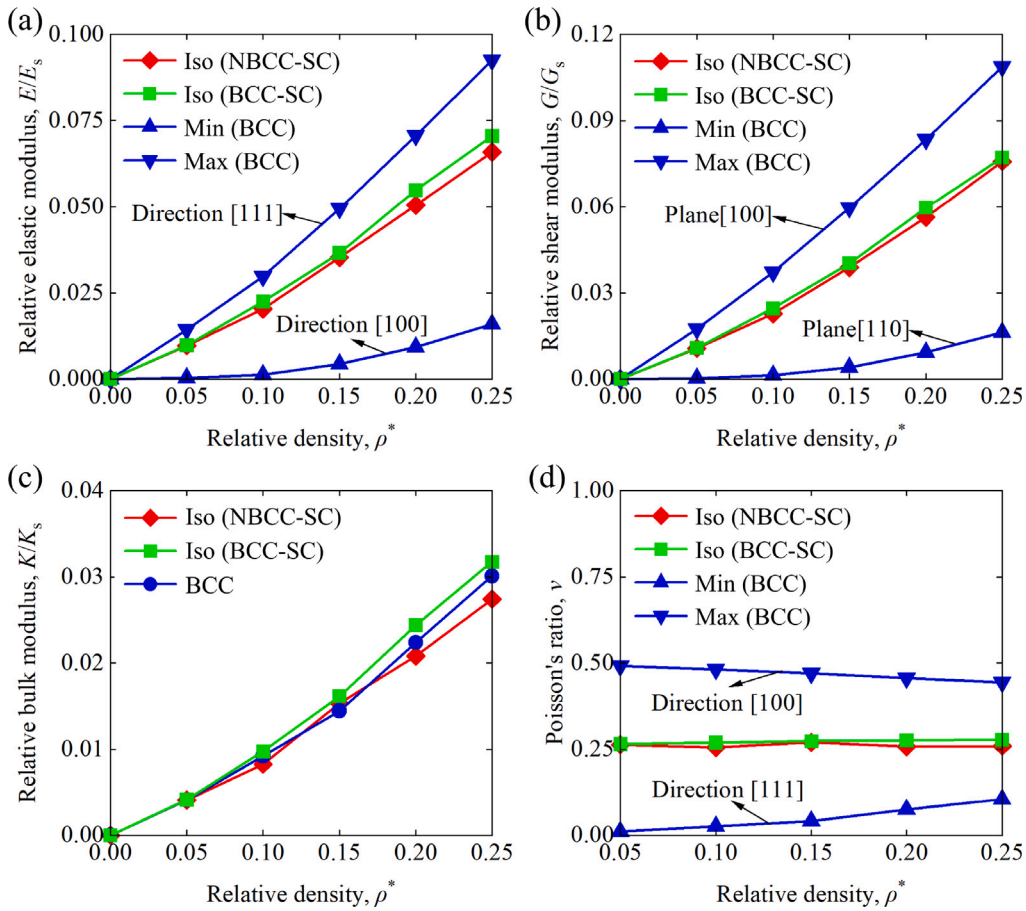

Fig. 6. Variation of (a) specific Young's modulus, (b) specific shear modulus, (c) specific bulk modulus, and (d) Poisson's ratio with relative density for the elastically isotropic NBCC–SC (optimized for isotropic yield strength) and BCC–SC lattices, and the BCC truss lattice.

0.05, the relative Young's modulus of the NBCC-SC lattice is 29 times that of the BCC lattice along the [100] direction, but 0.7 times that along the [111] direction. These ratios decline sharply (approximately exponentially) with density, reaching about 4 times that along direction [100] and 0.8 times that along direction [111] relative to the BCC lattice. A comparable anisotropy is also evident in the shear modulus: it increases slightly along [100] plane, from 0.6 to 0.7, but decreases dramatically along [110] plane, from 34 to 5, as the relative density increases from 0.05 to 0.25. The bulk modulus of the NBCC-SC lattice is comparable to that of the BCC lattice, and its value is approximately 0.9 times that of the latter. Regarding Poisson's ratio, the maximum and minimum values for the anisotropic BCC lattices are observed along the [100] and [111] directions, respectively. While the upper bound for the BCC lattice is about double that of the BCC-SC lattice, their sensitivity to relative density is markedly different: the BCC values decrease with increasing density, whereas the BCC-SC values increase slightly before stabilizing at roughly 0.26. At a relative density of 0.05, the lower bound value is nearly zero, subsequently increasing as the relative density rises.

A further comparative analysis between the elastically isotropic NBCC-SC and the conventional BCC-SC truss lattices is detailed in Fig. 6 and Fig. S4. Both lattice architectures demonstrate nearly identical effective elastic moduli and macroscopic Poisson's ratios. Furthermore, the effective elastic moduli of both structures are governed by closely analogous scaling laws with respect to relative density.

3.4. Large strain compression response and yield anisotropy

After satisfying the elastic-isotropy criteria, we assessed whether the inhomogeneous distribution strategy also reduces the loading-direction dependence of yield strength. The non-linear anisotropy is quantified by taking the ratio of the maximum and minimum yield strengths $\sigma_y^{max}/\sigma_y^{min}$ in all loading directions in the three-dimensional space. To probe the nonlinear response of the two lattice types, a large engineering compressive strain of −0.2 was applied to the numerical models along the three principal crystallographic directions: [100], [110], and [111]. Figs. 7 and 8 shows the stress–strain curves of NBCC-SC lattices at their optimal yield-strength isotropy. This state was achieved using offset ratios α of 0.4, 0.1, 0.1, 0.2 and 0.2, and 0.2, which correspond to relative densities ranging from 0.05 to 0.25. It should be noted that these 'optimal' configurations represent the best-performing designs identified within the discrete parameter space investigated ($\alpha \in \{0.1, 0.2, 0.3, 0.4, 0.5\}$ and $\rho^* \in \{0.05, 0.1, 0.15, 0.2, 0.25\}$), rather than solutions derived from a formal numerical optimization algorithm. For comparison, the stress–strain curves of the conventional BCC lattice under the same loading directions are included; the gray shaded region indicates the envelope of compressive responses of the BCC structure across different loading directions. The mechanical response is consistent across all loading directions: an initial linear elastic regime at small deformations is followed by slightly enhanced elastoplastic behavior and a nearly stable stress plateau.

The BCC lattice exhibits strong elastic and nonlinear anisotropy stemming from distinct deformation mechanisms that are direction-dependent. Compression along the [100] and [110] directions is characterized by a soft, bending-dominated mode, where stress concentrates at the nodes forming plastic hinges. Conversely, loading along the [111] direction activates a stiff, axial stress-dominated mode that compresses the diagonal struts. It is this stark contrast between bending and axial force-bearing mechanisms that gives rise to the pronounced anisotropic

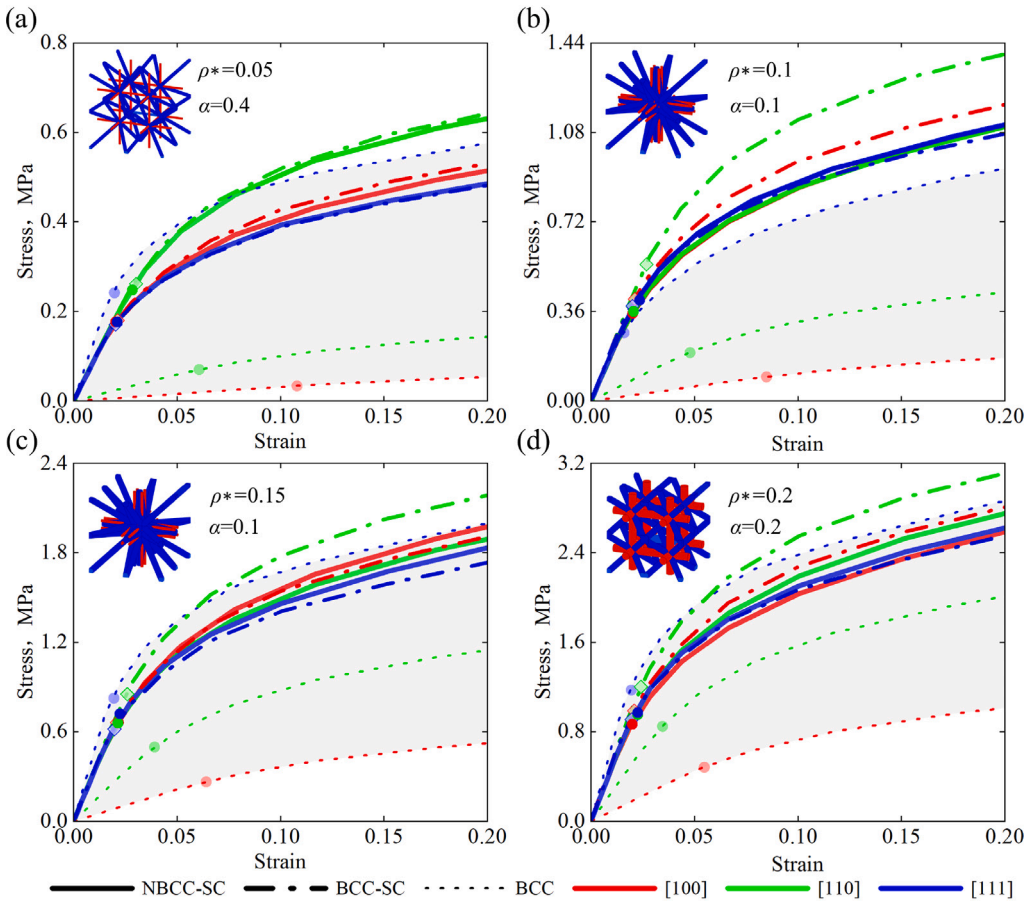

Fig. 7. (a)–(d) Compression responses of NBCC-SC , elastically isotropic BCC-SC and BCC truss lattices under [100], [110], and [111] loading across a relative density range of 0.05 to 0.2.

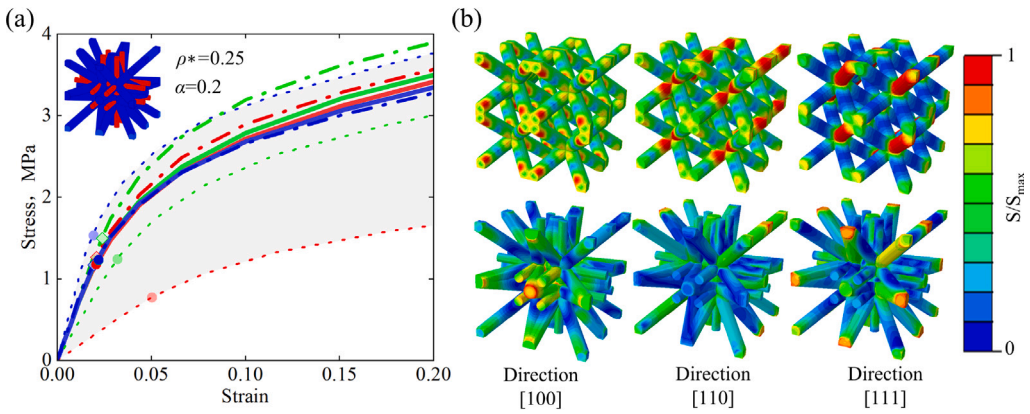

Fig. 8. (a) Simulated stress–strain responses and (b) deformation contours at 0.2% offset yield strain for NBCC-SC (α=0.2), BCC-SC and BCC truss lattices under loading along the three principal directions. All lattices have a relative density of 0.25. In the contour plots, S denotes the von Mises equivalent stress.

behavior of lattices, which is clearly illustrated in the deformation map at 0.2% offset yield strain (Fig. 8b). In contrast, the NBCC-SC lattice demonstrates perfect isotropy in its linear elastic regime and a nearly isotropic nonlinear response at relative densities of 0.1 and above. Even at a critically low density of 0.05, it maintains significantly greater isotropy than the BCC lattice. At this density, while the compression curves along the [110] and [111] directions show greater divergence due to an inherent structural feature required for elastic isotropy, the overall behavior remains more uniform. This is because the NBCC-SC lattice deforms via a similar stretching-dominated mode in all directions. This leads to a more uniform stress distribution and higher stress utilization efficiency, as each internal component is loaded more effectively. Its highly isotropic response is further explained by the structural constraints visible in Fig. 7b, which restrict deformation perpendicular to the loading axis. In most cases, the mechanical response of NBCC-SC lattices lies within the domain of values exhibited by BCC lattices. An exception occurs at a relative density of 0.1, where the compression response of the NBCC-SC lattice surpasses the upper performance bound of the BCC structures.

The compressive response of conventional elastically isotropic BCC–SC lattices is included in Figs. 7 and 8 to provide a comparative baseline. A significant advantage of the NBCC–SC architecture is its

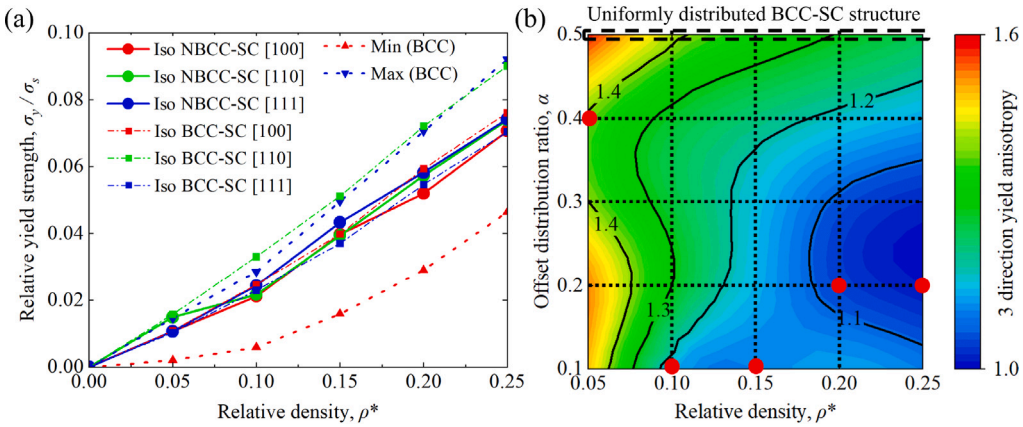

Fig. 9. (a) Evolution of yield strength with relative density for the elastically isotropic NBCC–SC and BCC–SC lattice along the [100], [110], and [111] directions, compared to the upper and lower bounds for BCC lattices. (b) Contour plots of the maximum-to-minimum yield-strength ratio for NBCC–SC lattices along the [100], [110], and [111] directions at relative densities of 0.05–0.25.

superior preservation of isotropy across the entire range of relative densities investigated. While the responses of both lattices converge at a low relative density of 0.05, the conventional BCC–SC exhibits a pronounced directional bias at higher densities. Specifically, the BCC–SC shows an increased compressive response along only two principal directions due to nonlinear anisotropy, whereas the NBCC–SC maintains a uniform, isotropic performance critical for multi-axial loading applications.

The dependency of the relative yield strength on relative density and loading direction for the optimal NBCC-SC and BCC-SC lattice is presented in Fig. 9a. The corresponding normalized relationships are provided in Fig. S4d. Yield strength increases with relative density for all structures. The BCC lattice shows considerable directional deviation, with the [100] direction following a quadratic strengthening trend and the [111] direction a more linear one. This can be explained by distinct deformation modes, analogous to those governing elastic modulus. Conversely, the NBCC-SC lattice demonstrates near-isotropic yield strength, with curves for the three principal directions almost coinciding. Although a slight hierarchy exists ([100] being the weakest and [111] the strongest), the overall increase is approximately linear. Importantly, the strength of the NBCC-SC structure approaches the maximum yield strength of BCC lattices across all loading directions over most of the density range. The conventional BCC-SC lattice demonstrates a comparable density-dependent scaling law. However, it diverges significantly from this isotropic behavior. Particularly at relative densities exceeding 0.1, the BCC-SC topology exhibits pronounced nonlinear anisotropy. Consequently, its yield response becomes highly direction-dependent, rather than uniformly elevated. This severe anisotropy dictates the macroscopic behavior, most notably manifesting as a significant divergence in the stress–strain trajectory along the [110] loading axis when compared to other principal directions.

Fig. 9b further illustrates the relationship between maximum and minimum yield stress ratios in three directions, demonstrating that nonlinear yield anisotropy during large deformation can be regulated through the offset distribution factor α. The blue regions indicate parameter combinations where the NBCC-SC lattice achieves near-isotropy in its nonlinear yield stage through offset regulation. Notably, the conventional elastically isotropic BCC-SC lattice (dashed box) corresponds to α=0.5. This article tested 25 groups in total, including 5 categories of offset values (0.1:0.1:0.5) and 5 categories of relative density (0.05:0.05:0.25). The term "optimal" here means that among all the possible offset values, the corresponding yield anisotropy value is better than the other four. The results show that the proposed inhomogeneous distribution strategy achieves superior nonlinear isotropy compared to uniform distribution across all relative densities, with optimal distribution forms marked by red dots in the figure. Specifically, at a relative density of 0.05, the inhomogeneous distribution with α=0.4 yields the best near isotropy in the nonlinear stage, as confirmed by the contour plots. At relative densities of 0.1 and 0.15, α=0.1 is optimal, while at relative densities of 0.2 and 0.25, α=0.2 provides the best performance. With increasing relative density, the optimal α values converge to approximately 0.2–0.3.

Fig. 10 and Fig.S5 further quantifies the yield anisotropy, showing the NBCC–SC lattice exhibits a significantly lower 31-directional yield-stress ratio than the uniform BCC-SC lattice, confirming its enhanced isotropy. In the uniform BCC-SC lattice, the specific yield stress is highest along the [110] direction and lowest along the [111] direction. For the lattice with a relative density of 0.05, the optimal inhomogeneous distribution is achieved when α = 0.4, with the ratio decreasing from 1.53 (α = 0.5) to 1.4,The weakest and strongest yield directions are [111] and [110]. More generally, the 31-direction ratio decreases at all relative densities with the proposed inhomogeneous distributions. As α decreases to 0.3, the 31-directional maximum-to-minimum yield-stress ratios further decline for relative densities no less than 0.1. At α = 0.2 the optimal distribution for high relative densities (0.2 and 0.25) is reached: the ratio falls from 1.32 to 1.12 at a relative density of 0.2, with the weakest and strongest yield directions being [100] and [29, 19, 10], and from 1.28 to 1.05 at a relative density of 0.25, with the weakest and strongest directions being [100] and [213, 100, 0]. These values represent one of the most nearly isotropic yield behaviors reported for architected lattice materials, providing a balanced performance relative to previously documented architectures. The optimal distribution was achieved with an inhomogeneity ratio of α = 0.1, which significantly decreased the anisotropic ratio—from 1.44 to 1.15 for a relative density of 0.1, with the weakest and strongest yield directions being [100] and [19, 19, 10], and from 1.38 to 1.1 for 0.15, with the weakest and strongest directions being [110] and [100].

4. Experiments

To verify the accuracy of the simulation results, NBCC-SC (α=0.2) lattice samples with a relative density of 0.25 were fabricated from PA12 material using Multi Jet Fusion 3D printing. The influence of loading direction was evaluated by testing samples oriented along the crystallographic [100] and [110] directions. For each configuration, two samples were produced, each containing a 4 × 4 × 4 array of unit cells (Fig. 11). To ensure experimental accuracy, the [100]-oriented sample was created from a larger 5 × 5 × 5 array, from which the central 4 × 4 × 4 units were selected to minimize the number of unstressed free ends at the sample boundaries. The [110] unit cell was constructed by diagonally sectioning a 2 × 2 × 1 [100] unit cell. The geometric parameters of the printed samples are summarized in Table 1,

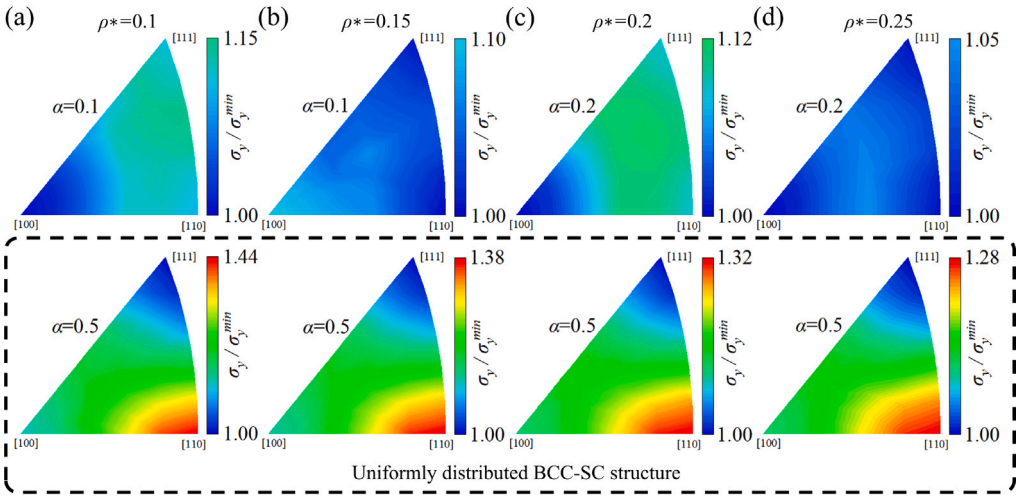

Fig. 10. (a)–(b) Polar plots quantifying the directional yield strength of optimal NBCC-SC lattices versus their uniform BCC-SC counterparts at relative densities of 0.1–0.25.

Table 1
Measured dimensions and mass error of the printed specimens.

Type	Crystallographic direction	Direction 1 (mm)	Direction 2 (mm)	Direction 3 (mm)	Relative density (%)	Standard deviations (%)
NBCC-SC (α=0.2)	[100]	80.30	80.23	80.68	26.70	6.8
		80.28	80.25	80.48	26.52	6.08
	[110]	80.31	113.42	113.45	26.89	7.56
		80.33	113.39	113.48	26.98	7.92

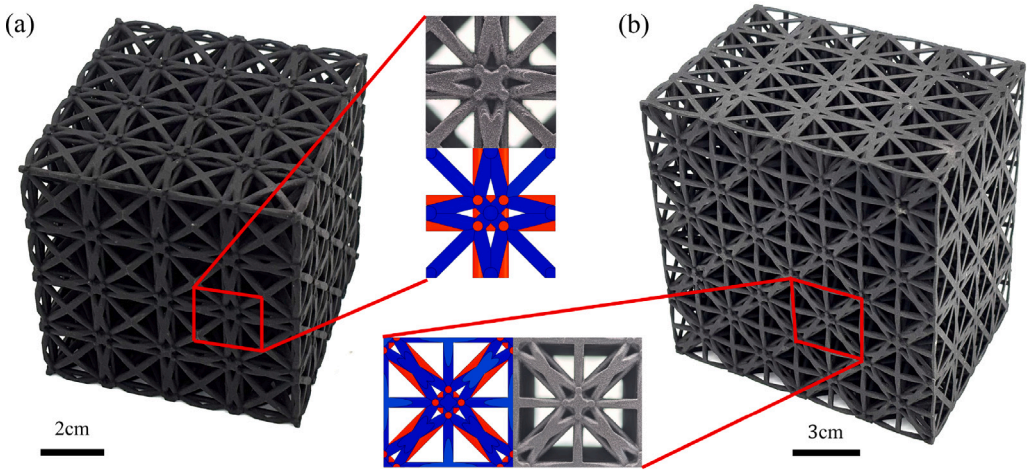

Fig. 11. Dimetric and close-up views of the NBCC-SC (α =0.2) with a target relative density of 0.25. The actual measured densities are 0.2670 and 0.2652 for the [100] samples, and 0.2689 and 0.2698 for the [110] samples. The views are oriented along the: (a) [100] and (b) [110] directions.

with truss diameters calculated using the previously derived formulas. The slight overestimation in relative density is primarily attributed to residual powder trapped within the lattice structure during the printing process.

Upon fabrication, the samples underwent compression testing using an MTS322 testing machine with a 500 kN load cell at a constant engineering strain rate of $0.001s^{-1}$. To ensure uniform loading and prevent out-of-plane instability, each sample was carefully centered on the testing platen. A preload was applied to eliminate any initial slippage between the sample and the platen surfaces. The deformation process was monitored using digital image correlation, for which the sample surfaces were prepared with a speckle pattern (average speckle radius: 60 μ m). Engineering stress was calculated from the applied force divided by the sample's cross-sectional area, and engineering strain was derived from the platen displacement divided by the original sample height. Fig. 12 presents the experimental compressive stress–strain curves and corresponding deformation sequences for the NBCC-SC (α=0.2) lattices. The responses for both the [100] and [110] directions exhibit an initial linear elastic region, followed by nonlinear hardening until the peak stress, with yield strengths of 1.70 MPa and 1.69 MPa, respectively. The near-overlap of the experimental curves prior to fracture confirms the near-isotropic properties predicted by the simulations, showing excellent agreement between experiments and simulations. However, the curves for the two directions begin to deviate at a strain of approximately 0.075, coinciding with the fracture of micro-struts. When loaded along the [100] and [110] directions, the structure reached peak stresses of 2.5 MPa and 2.6 MPa, respectively, at a strain of about 0.08. With further loading, both samples underwent catastrophic failure, characterized by non-periodic stress oscillations, a

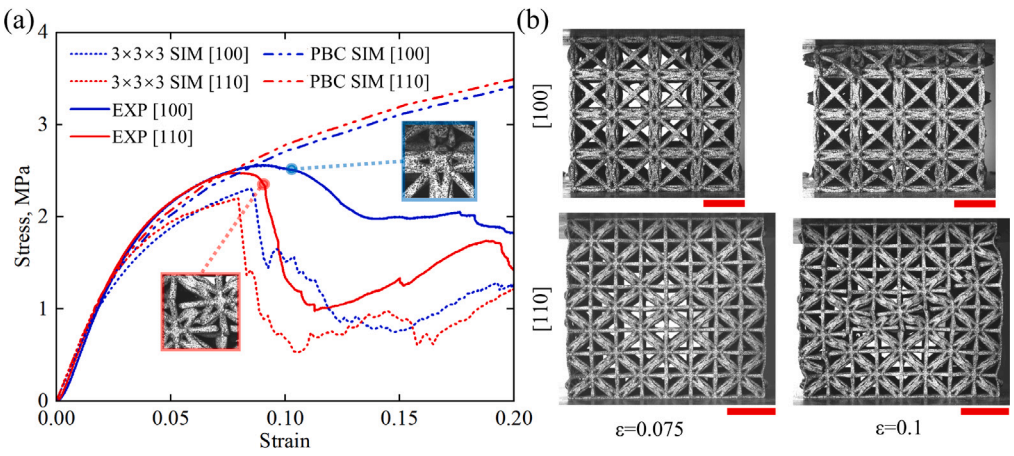

Fig. 12. (a) Experimental engineering stress–strain curves from uniaxial compression tests on NBCC-SC lattices, showing yield points and compared with simulation results. (b) Deformation morphology evolution at selected strains for loading along the [100] and [110] directions. Scale bars represent 20 mm ([100]) and 28.3 mm ([110]).

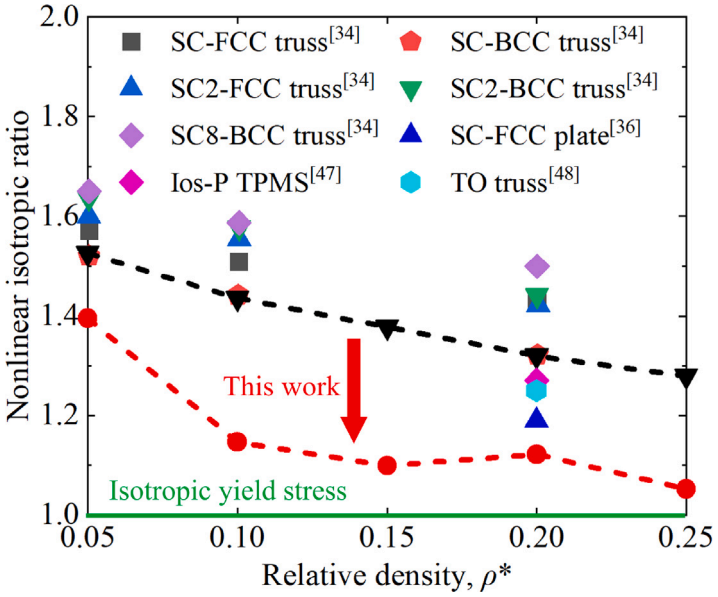

Fig. 13. Comparison of yield anisotropy between non-uniformly distributed NBCC-SC structures, uniformly distributed BCC-SC structures, and other elastically isotropic lattices.

phenomenon not predicted by the unit cell simulations. To address this, multi-cell simulations were conducted, which exhibit a compressive response that closely aligns with the experimental trends and successfully predict the fracture strain at which the stress–strain curves drop. While the simulations slightly underestimate the compressive response, this is likely due to the finite number of unit cells modeled. While increasing the unit cell count would further reduce the discrepancy between simulation and experiment, the computational cost is prohibitive. Such discrepancies could be mitigated by replacing the brittle PA with a more ductile and malleable material, such as 316L stainless steel.

To further assess their significance within the lattice family, we comprehensively compared the yield anisotropy ratios of the NBCC-SC lattice against other elastically isotropic lattices (See Fig. 13) (Tancogne-Dejean and Mohr, 2018b; Tancogne-Dejean et al., 2018; Daynes, 2024; Alkhatib et al., 2023). The traditional uniform BCC-SC lattice exhibits a steady decline in anisotropy ratio with increasing relative density,a trend consistent with findings reported by Tancogne-Dejean and Mohr (2018b). In contrast, the NBCC-SC lattice, designed with a variable distribution strategy, shows an initial decrease in anisotropy ratio, followed by a slight increase at a relative density of 0.2. Within the relative density range of 0.1 to 0.2, the anisotropy ratio remains near 1.1, indicating highly limited yield anisotropy. This performance is comparable to the RD plate lattice and superior to other elastically isotropic truss, shell, and SC-FCC plate lattices. Notably, at a relative density of 0.25, the ratio approaches 1.05, positioning the NBCC-SC architecture among the most nearly isotropic configurations observed in the nonlinear regime to date. These results confirm that the proposed inhomogeneous strategy effectively controls anisotropy in the nonlinear yield stage, offering a novel method for tailoring load-bearing capacity and energy absorption in non-deterministic service environments.

5. Conclusion

This work presents a novel offset asymmetry strategy that extends material isotropy into the large strain deformation regime, advancing beyond the elastic isotropy offered by common approaches. The method involves offsetting the central node of a 2 × 2 × 2 cubic unit cell along the diagonal direction, hybridizing simple cubic and body-centered cubic structures into a non-uniform BCC-SC lattice with a tunable offset ratio. Numerical and experimental results confirm

that tailoring this geometrical parameter enables not only stretching-dominated isotropic stiffness but also a near-isotropic inelastic large-deformation response, outperforming uniform lattices. Characterized by a near-unity yield strength anisotropic ratio of just 1.05, the optimal NBCC-SC structure represents one of the most isotropic lattice reported in the nonlinear regime to date. Remarkably, the optimal NBCC-SC lattice performs near the upper theoretical bound of BCC lattices in all directions while far exceeding the lower bound. This inhomogeneous design strategy provides a powerful method for controlling linear and nonlinear anisotropy, with promising applications in aerospace, biomedical engineering, and other fields requiring tailored mechanical performance.

CRediT authorship contribution statement

Xudong Huang: Writing – original draft, Visualization, Validation, Investigation, Data curation, Conceptualization. **Penghui Yu:** Validation, Software, Methodology, Investigation. **Peijie Zhang:** Validation, Formal analysis, Data curation. **Xueyan Chen:** Writing – review & editing, Validation, Supervision, Funding acquisition, Data curation, Conceptualization. **Huifeng Tan:** Writing – review & editing, Validation, Supervision, Conceptualization. **Muamer Kadic:** Writing – review & editing, Validation, Supervision, Conceptualization.

Declaration of competing interest

The authors declare that they have no known competing financial interests or personal relationships that could have appeared to influence the work reported in this paper.

Acknowledgments

This work was supported by the National Nature Science Foundation of China under Grant No. 12572152, Science Foundation of National Key Laboratory of Science and Technology on Advanced Composites in Special Environments and China Postdoctoral Science Foundation (2025T181142 and 2023M730865).

Appendix A. Supplementary data

Supplementary material related to this article can be found online at https://doi.org/10.1016/j.ijsolstr.2026.114096.

Data availability

Data will be made available on request.

References

Alkhatib, S.E., Karrech, A., Sercombe, T.B., 2023. Isotropic energy absorption of topology optimized lattice structure. Thin-Walled Struct. 182, 110220.
Berger, J., Wadley, H., McMeeking, R., 2017. Mechanical metamaterials at the theoretical limit of isotropic elastic stiffness. Nature 543 (7646), 533–537.
Bonatti, C., Mohr, D., 2019. Mechanical performance of additively-manufactured anisotropic and isotropic smooth shell-lattice materials: Simulations & experiments. J. Mech. Phys. Solids 122, 1–26.
Bückmann, T., Schittny, R., Thiel, M., Kadic, M., Milton, G.W., Wegener, M., 2014. On three-dimensional dilational elastic metamaterials. New J. Phys. 16 (3), 033032.
Chen, X., Ji, Q., Martinez, J.A.I., Tan, H., Ulliac, G., Laude, V., Kadic, M., 2022a. Closed tubular mechanical metamaterial as lightweight load-bearing structure and energy absorber. J. Mech. Phys. Solids 167, 104957.
Chen, X., Ji, Q., Wei, J., Tan, H., Yu, J., Zhang, P., Laude, V., Kadic, M., 2020a. Light-weight shell-lattice metamaterials for mechanical shock absorption. Int. J. Mech. Sci. 169, 105288.
Chen, X., Moughames, J., Ji, Q., Martínez, J.A.I., Tan, H., Adrar, S., Laforge, N., Cote, J.-M., Euphrasie, S., Ulliac, G., et al., 2020b. Optimal isotropic, reusable truss lattice material with near-zero Poisson's ratio. Extrem. Mech. Lett. 41, 101048.
Chen, X., Moughames, J., Ji, Q., Martínez, J.A.I., Tan, H., Ulliac, G., Laude, V., Kadic, M., 2022b. 3D lightweight mechanical metamaterial with nearly isotropic inelastic large deformation response. J. Mech. Phys. Solids 169, 105057.
Chen, X., Tan, H., 2018. An effective length model for octet lattice. Int. J. Mech. Sci. 140, 279–287.
Chen, X., Yu, P., Ma, H., Zhang, P., Ding, C., Liu, S., Zhang, X., Tan, H., 2024. A class of elastic isotropic plate lattice materials with near-isotropic yield stress. Acta Mater. 276, 120085.
Daynes, S., 2024. Isotropic cellular structure design strategies based on triply periodic minimal surfaces. Addit. Manuf. 81, 104010.
Daynes, S., Feih, S., 2025. Functionally graded lattice structures with tailored stiffness and energy absorption. Int. J. Mech. Sci. 285, 109861.
Deshpande, V., Ashby, M., Fleck, N., 2001a. Foam topology: bending versus stretching dominated architectures. Acta Mater. 49 (6), 1035–1040.
Deshpande, V.S., Fleck, N.A., Ashby, M.F., 2001b. Effective properties of the octet-truss lattice material. J. Mech. Phys. Solids 49 (8), 1747–1769.
Dudek, K.K., Duncan, O., Martínez, J.A.I., Kadic, M., 2025. Mechanical metamaterial-based structure with magnetically controlled nonreversibility and nonreciprocity for programmable locomotion. Adv. Sci. e03088.
Gurtner, G., Durand, M., 2014. Stiffest elastic networks. Proc. R. Soc. A: Math. Phys. Eng. Sci. 470 (2164), 20130611.
Jiao, P., Mueller, J., Raney, J.R., Zheng, X., Alavi, A.H., 2023. Mechanical metamaterials and beyond. Nat. Commun. 14 (1), 6004.
Li, S., Wongsto, A., 2004. Unit cells for micromechanical analyses of particle-reinforced composites. Mech. Mater. 36 (7), 543–572.
Liu, X., Chen, S., Wang, B., Tan, X., Cao, B., Yu, L., 2025a. A mechanical metamaterial with real-time tunable bandgap based on pneumatic actuation. Int. J. Mech. Sci. 289, 110045.
Liu, W., Ennis, B., Coulais, C., 2025b. Tuning the buckling sequences of metamaterials using plasticity. J. Mech. Phys. Solids 196, 106019.
Liu, W., Janbaz, S., Dykstra, D., Ennis, B., Coulais, C., 2024a. Harnessing plasticity in sequential metamaterials for ideal shock absorption. Nature 634 (8035), 842–847.
Liu, H., Ma, W.W.S., Ding, J., Qu, S., Li, R., Ge, Q., Wang, M.Y., Song, X., 2024b. Hierarchical triply periodic minimal surface shell lattices with superior isotropic elasticity: Design guidelines, fabrication, and validation. Addit. Manuf. 94, 104451.
Ma, Q., Zhang, L., Ding, J., Qu, S., Fu, J., Zhou, M., Fu, M., Song, X., Wang, M., 2021. Elastically-isotropic open-cell minimal surface shell lattices with superior stiffness via variable thickness design. Addit. Manuf 47, 2021.
Maurin, F., Claeys, C., Van Belle, L., Desmet, W., 2017. Bloch theorem with revised boundary conditions applied to glide, screw and rotational symmetric structures. Comput. Methods Appl. Mech. Engrg. 318, 497–513.
Mizzi, L., Dudek, K.K., Frassineti, A., Spaggiari, A., Ulliac, G., Kadic, M., 2025. Lightweight 3D hierarchical metamaterial microlattices. Adv. Sci. 12 (20), 2410293.
Schaedler, T.A., Jacobsen, A.J., Torrents, A., Sorensen, A.E., Lian, J., Greer, J.R., Valdevit, L., Carter, W.B., 2011. Ultralight metallic microlattices. Science 334 (6058), 962–965.
Tan, X., Cao, B., Liu, W., Ji, C., Wang, B., Li, S., 2024a. Odd mechanical metamaterials with simultaneously expanding or contracting under both compression and tension. Thin-Walled Struct. 203, 112225.
Tan, X., Cao, B., Liu, X., Zhu, S., Chen, S., Kadic, M., Wang, B., 2024b. Negative stiffness mechanical metamaterials: a review. Smart Mater. Struct..
Tan, X., Ma, J., Liu, S., Cao, B., Chen, X., Wang, B., Kadic, M., 2026. Design, fabrication, and characterization of solid–liquid dual-state mechanical metamaterials. Int. J. Solids Struct. 113865.
Tancogne-Dejean, T., Diamantopoulou, M., Gorji, M.B., Bonatti, C., Mohr, D., 2018. 3D plate-lattices: an emerging class of low-density metamaterial exhibiting optimal isotropic stiffness. Adv. Mater. 30 (45), 1803334.
Tancogne-Dejean, T., Mohr, D., 2018a. Elastically-isotropic elementary cubic lattices composed of tailored hollow beams. Extrem. Mech. Lett. 22, 13–18.
Tancogne-Dejean, T., Mohr, D., 2018b. Elastically-isotropic truss lattice materials of reduced plastic anisotropy. Int. J. Solids Struct. 138, 24–39.
Tsang, T., Park, H.-Y., 1983. Sound velocity anisotropy in cubic crystals. Phys. Lett. A 99 (8), 377–380.
Voigt, W., 1910. Lehrbuch Der Kristallphysik:(mit Ausschluss Der Kristalloptik), vol. 34, BG Teubner.
Wang, L., Iglesias Martínez, J.A., Dudek, K.K., Ulliac, G., Niu, X., Zou, Y., Wang, B., Laude, V., Kadic, M., 2024. Multistep and elastically stable mechanical metamaterials. J. Appl. Mech. 91 (11), 111002.
Wang, Y., Xu, F., Gao, H., Li, X., 2023. Elastically isotropic truss-plate-hybrid hierarchical microlattices with enhanced modulus and strength. Small 19 (18), 2206024.
Wei, X., Jiao, Y., Wang, Y., Yan, C., Han, J., Xiong, J., 2024a. Surface matching design of carbon fiber composite honeycomb. J. Mech. Phys. Solids 193, 105890.
Wei, X., Wang, Y., Jiao, Y., Xue, P., Han, J., Xiong, J., 2024b. Bending behaviors of carbon fiber composite honeycomb cores with various in-plane stiffness. Compos. Struct. 347, 118448.
Xu, S., Shen, J., Zhou, S., Huang, X., Xie, Y.M., 2016. Design of lattice structures with controlled anisotropy. Mater. Des. 93, 443–447.

Yan, S., Liu, W., Tan, X., Meng, Z., Luo, W., Jin, H., Wen, Y., Sun, J., Wu, L., Zhou, J., 2024. Bio-inspired mechanical metamaterial with ultrahigh load-bearing capacity for energy dissipation. Mater. Today 77, 11–18.

Yu, P., Zhang, P., Ji, Q., Yang, F., Tan, X., Chen, X., Tan, H., Laude, V., Kadic, M., 2024. A multi-step auxetic metamaterial with instability regulation. Int. J. Solids Struct. 305, 113040.

Yu, P., Zhang, P., Ma, H., Chen, X., Tan, H., Kadic, M., 2025. An alternating collinear tubular lattice material with enhanced energy absorption. Int. J. Solids Struct. 113426.

Zhang, P., Chen, X., Yu, P., Zhao, K., Ma, H., Liu, S., Tan, H., Laude, V., Kadic, M., 2025a. Grid hollow octet truss lattices that are stable at low relative density. J. Mech. Phys. Solids 197, 106068.

Zhang, P., Chen, X., Yu, P., Zhao, K., Yin, H., Wan, C., Tan, H., Kadic, M., 2025b. Shell-lattice metamaterials with intrinsic contact stabilization for exceptional mechanical performance and nonlinear stability. J. Mech. Phys. Solids 106467.

Zhang, J., Xie, S., Jing, K., Wang, H., Li, T., He, G., 2024. Study on isotropic design of triply periodic minimal surface structures under an elastic modulus compensation mechanism. Compos. Struct. 342, 118266.

Zhang, P., Yu, P., Zhang, R., Chen, X., Tan, H., 2023. Grid octet truss lattice materials for energy absorption. Int. J. Mech. Sci. 259, 108616.

Zhao, M., Li, X., Zhang, D.Z., Zhai, W., 2023. Geometry effect on mechanical properties and elastic isotropy optimization of bamboo-inspired lattice structures. Addit. Manuf. 64, 103438.

Zheng, X., Lee, H., Weisgraber, T.H., Shusteff, M., DeOtte, J., Duoss, E.B., Kuntz, J.D., Biener, M.M., Ge, Q., Jackson, J.A., et al., 2014. Ultralight, ultrastiff mechanical metamaterials. Science 344 (6190), 1373–1377.